# Supporting Information for

# Severe Dirac Mass Gap Suppression in $Sb_2Te_3$-based Quantum Anomalous Hall Materials

Yi Xue Chong[1,2*], Xiaolong Liu[1,3*], Rahul Sharma[1,2], Andrey Kostin[1], Genda Gu[2], K. Fujita[2], J.C. Séamus Davis[1,4,5,#] and Peter O. Sprau[1,6]

*1. LASSP, Department of Physics, Cornell University, Ithaca, NY 14853, USA*
*2. CMPMS Department, Brookhaven National Laboratory, Upton, NY 11973, USA*
*3. Kavli Institute at Cornell, Cornell University, Ithaca, NY 14853, USA*
*4. Department of Physics, University College Cork, Cork T12R5C, IE*
*5. Clarendon Laboratory, University of Oxford, Oxford, OX1 3PU, UK*
*6. Advanced Development Center, ASML, Wilton, CT 06897, USA.*

* Y.X.C and X.L contributed equally to this work.
# Correspondence should be addressed to: jcseamusdavis@gmail.com

## 1. Determination of Fermi velocities and the Dirac point

In general, the LL energies $E_n$ in a Dirac surface state obey:

$$E_n = E_D + \lambda\sqrt{2e\hbar B|n|v_F^2 + \Delta^2} \text{ for } n \neq 0 \quad (1)$$

, where $E_D$ is the Dirac point, $B$ is the external magnetic field, $v_F$ is Fermi velocity, which could differ between the two Dirac cones, and $\Delta$ is the Dirac-mass Gao. Here, $\lambda = 1$ for $n > 0$, and $\lambda = -1$ for $n < 0$. The 0th LL is at $E_0 = E_D \pm \Delta$, where the sign depends on the relative direction of the sample magnetization and the external magnetic field. For $(Bi_{0.1}Sb_{0.9})_2Te_3$ where $\Delta = 0$, the following expressions could be obtained:

$$E_D = E_0 \quad (2)$$

$$E_1 = E_D + \sqrt{2e\hbar B}v_{F-T} \quad (3)$$

$$E_{-1} = E_D - \sqrt{2e\hbar B}v_{F-B} \quad (4)$$

For $Cr_{0.08}(Bi_{0.1}Sb_{0.9})_{1.92}Te_3$ where $\Delta \neq 0$, the following expressions could be obtained using LLs with $n$ = -2, -1, 0, and 1:

$$E_D = \frac{E_0^2 + E_{-2}^2 - 2E_{-1}^2}{2(E_0 + E_{-2} - 2E_{-1})} \quad (5)$$

$$\Delta = E_0 - E_D \quad (6)$$

$$v_{F-T} = \sqrt{\frac{(E_1 - E_D)^2 - \Delta^2}{2e\hbar B}} \quad (7)$$

$$v_{F-B} = \sqrt{\frac{(E_D - E_{-1})^2 - \Delta^2}{2e\hbar B}} \quad (8)$$

Therefore, the quantities above could be obtained using LLs experimentally determined. Similarly, the above quantities could be obtained by using LLs with $n$ = -1, 0, 1, and 2:

$$E_D = \frac{E_0^2 + E_2^2 - 2E_1^2}{2(E_0 + E_2 - 2E_1)} \quad (9)$$

$$\Delta = E_0 - E_D \quad (10)$$

$$v_{F-T} = \sqrt{\frac{(E_1 - E_D)^2 - \Delta^2}{2e\hbar B}} \quad (11)$$

$$v_{F-B} = \sqrt{\frac{(E_D - E_{-1})^2 - \Delta^2}{2e\hbar B}} \quad (12)$$

Both approaches yield similar results and the results are also consistent with zero-field measurements on $E_D$ (see Fig. S7), validating extraction of physical quantities using LL spectroscopy.

**2. Discussion on the narrower distribution of higher Landau levels (LLs) compared to that of the 0th LL**

For $(Bi_{0.1}Sb_{0.9})_2Te_3$,

$$\frac{\delta E_n}{\delta E_0} = 1 + \sqrt{2e\hbar Bn}\frac{\delta v_{F-T}}{\delta E_D} \text{ for } n > 0 \quad (13)$$

$$\frac{\delta E_n}{\delta E_0} = 1 - \sqrt{2e\hbar B|n|}\frac{\delta v_{F-B}}{\delta E_D} \text{ for } n < 0 \quad (14)$$

, where $\delta$ denotes variations. Since $v_{F-T}(\boldsymbol{r})$ and $v_{F-B}(\boldsymbol{r})$ anticorrelates and correlates with $E_D(\boldsymbol{r})$ as shown in Fig. 3 and Fig. S3, we know that $\frac{\delta v_{F-T}}{\delta E_D} < 0$ and $\frac{\delta v_{F-B}}{\delta E_D} > 0$. The spatial variation of $v_F$ is still small enough such that $E_n$ for $n \neq 0$ shift in the same direction as $E_0$ (or $E_D$) as a result of the Dirac cones being shifted up and down due to $E_D$ fluctuations (Fig. S4). Therefore, $0 < \frac{\delta E_n}{\delta E_0} < 1$ for both $n > 0$ and $n < 0$. From equation (13) and (14), we see that the $\frac{\delta E_n}{\delta E_0}$ decreases as $n$ increases for both $n > 0$ and $n < 0$, thus explaining the smaller distribution widths of the LLs at larger $n$ shown in Fig. S4. In addition, the spatial extent of the LL eigenstates scale with $\sqrt{n}$. It is therefore expected a spatial averaging

effect is stronger in higher LLs, contributing to lower measured energy fluctuations. For this reason, lower LLs with n=-2, -1, 0, 1, 2 are used for mapping physical quantities for highest spatial resolution.

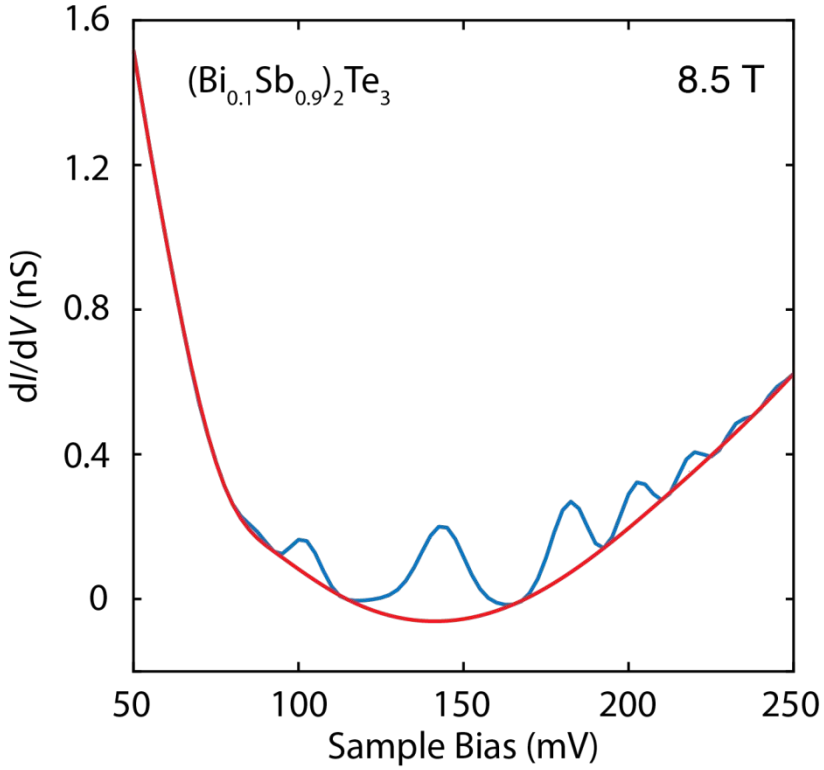


**Figure S1**. Raw LL spectrum of $(Bi_{0.1}Sb_{0.9})_2Te_3$ (blue) and its uniform background used for subtraction (red).

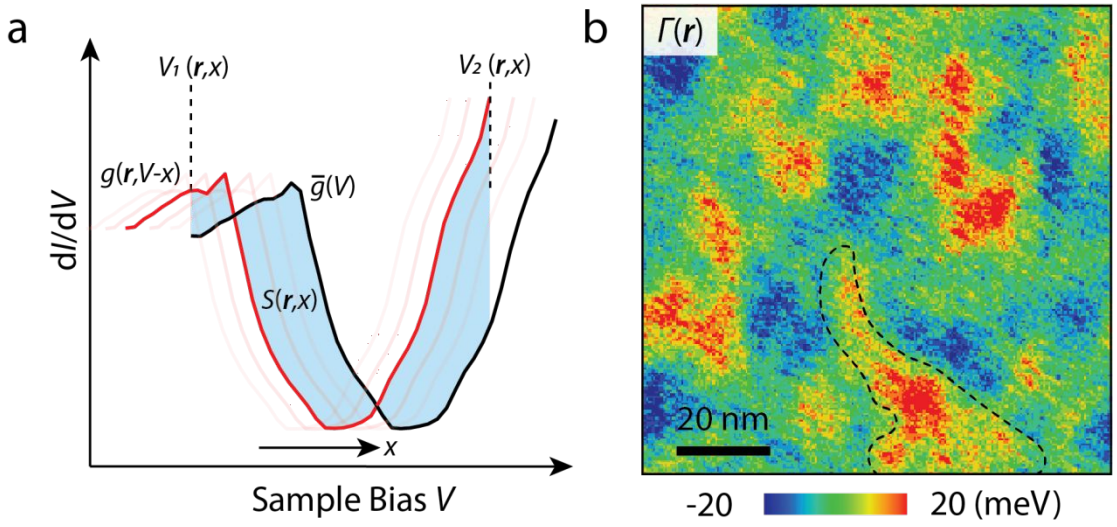


**Figure S2**. Bulk band shift as a function of position in $(Bi_{0.1}Sb_{0.9})_2Te_3$. (a) Schematic of how the rigid bulk band shift is determined. The black curve represents the spatially averaged differential conductance curve $\bar{g}(V) = \overline{dI/dV}$, and the red curve represents a local differential conductance $g(\boldsymbol{r},V) = dI(\boldsymbol{r},V)/dV$ with a shift in voltage by $x$. The two curves have an overlapping energy range from $V_1(\boldsymbol{r},x)$ to $V_2(\boldsymbol{r},x)$. The overlapping area of the two curves $S(\boldsymbol{r},x)$ is defined as (i.e., the blue area):

$$S(\boldsymbol{r},x) = \int_{V_1(\boldsymbol{r},x)}^{V_2(\boldsymbol{r},x)} |\bar{g}(V) - g(\boldsymbol{r},V-x)| dV \qquad (15)$$

Then the rigid band shift $\Gamma(\boldsymbol{r})$ at each position $\boldsymbol{r}$ is determined as the value of $x$ that minimizes the normalized overlapping area $\frac{S(\boldsymbol{r},x)}{V_2(\boldsymbol{r},x)-V_1(\boldsymbol{r},x)}$. (b) Determined rigid band shift in the same area as shown in Fig. 1c.

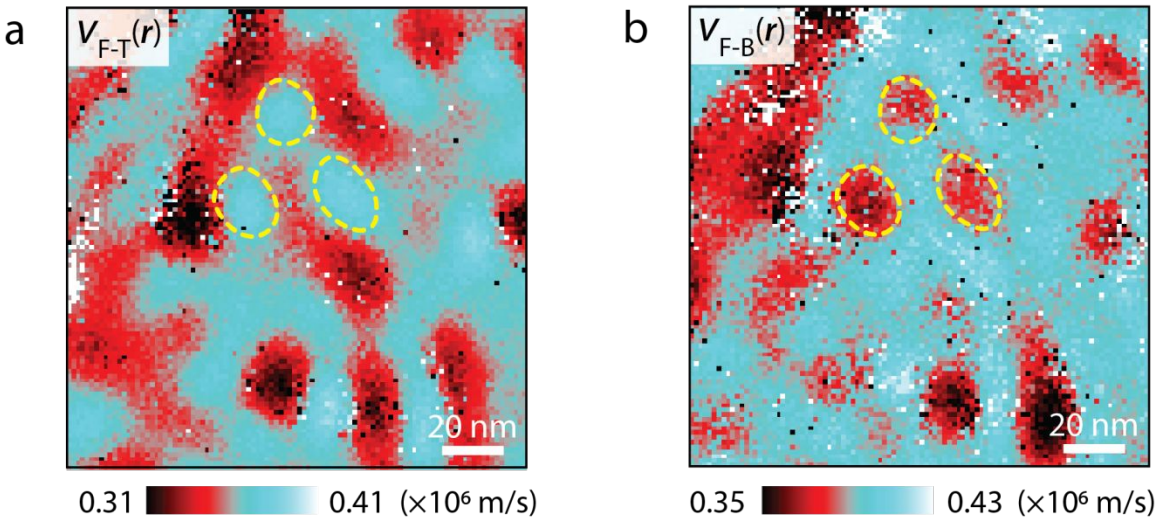


**Figure S3**. (a,b) Spatial maps of $V_{F-T}$, and $V_{F-B}$, respectively in $(Bi_{0.1}Sb_{0.9})_2Te_3$. Both Fermi velocities show spatial fluctuations, and $v_{F-T}(\boldsymbol{r})$ and $v_{F-B}(\boldsymbol{r})$ show clear anticorrelation with each other. The yellow dashed circles are to guide the eye.

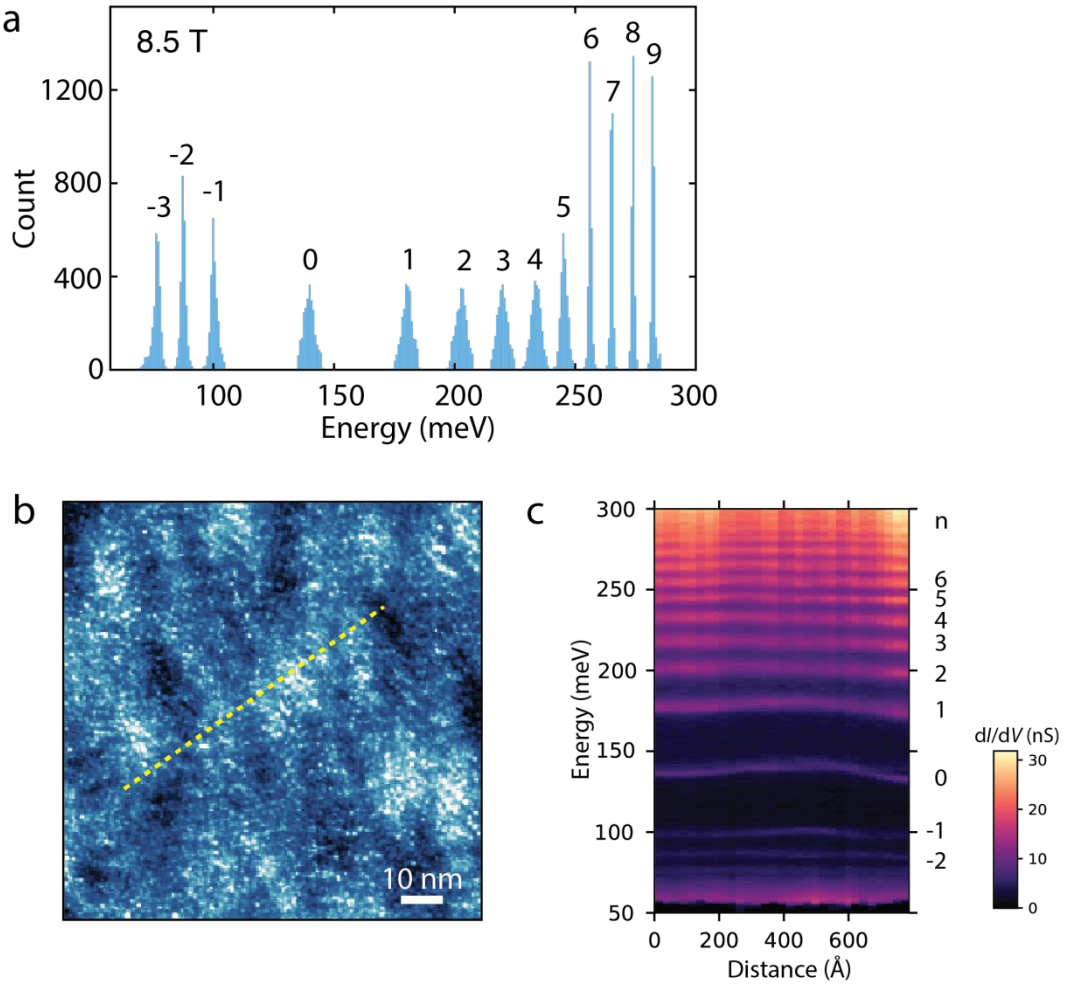


**Figure S4**. Evolution of LLs in $(Bi_{0.1}Sb_{0.9})_2Te_3$. (a) Histogram of the LLs of $(Bi_{0.1}Sb_{0.9})_2Te_3$ obtained in a 8.5 T magnetic field. (b) A topographic image of $(Bi_{0.1}Sb_{0.9})_2Te_3$, where the yellow dashed line denotes where a series of LL spectra were taken shown in (c). Along the line, fluctuations of the LL energies are clearly visible. However, the LLs shifts in the same direction which is most clearly seen for $n = -1, 0, 1, 2$.

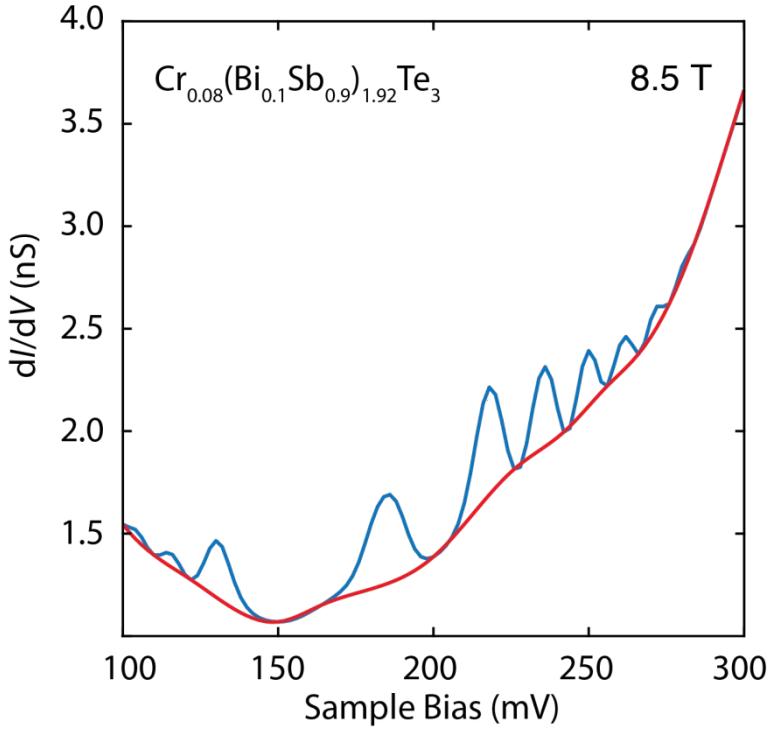


**Figure S5**. Raw LL spectrum of $Cr_{0.08}(Bi_{0.1}Sb_{0.9})_{1.92}Te_3$ (blue) and its uniform background used for subtraction (red).

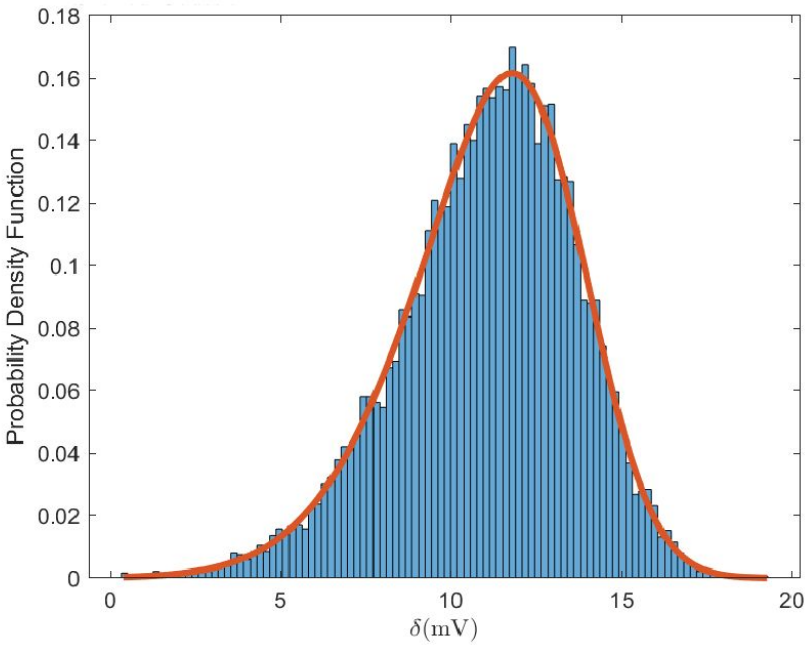


**Figure S6**. Skewed normal distribution of simulated $\delta(\boldsymbol{r})$. Using the mean and standard deviation values of experimental $E_D(\boldsymbol{r})$ and $\Delta(\boldsymbol{r})$, a set of simulated $E_D(\boldsymbol{r})$ and $\Delta(\boldsymbol{r})$ is drawn from their respective normal distributions. This set of simulated $\delta(\boldsymbol{r})$ is then computed using the same procedure explained in the main text. The histogram is fitted with a skewed normal distribution, resulting in $\mu = 13.74\, meV$, $\sigma = 3.70\, meV$, $\alpha = -2.07$, which closely match experimental results shown in Fig. 4.

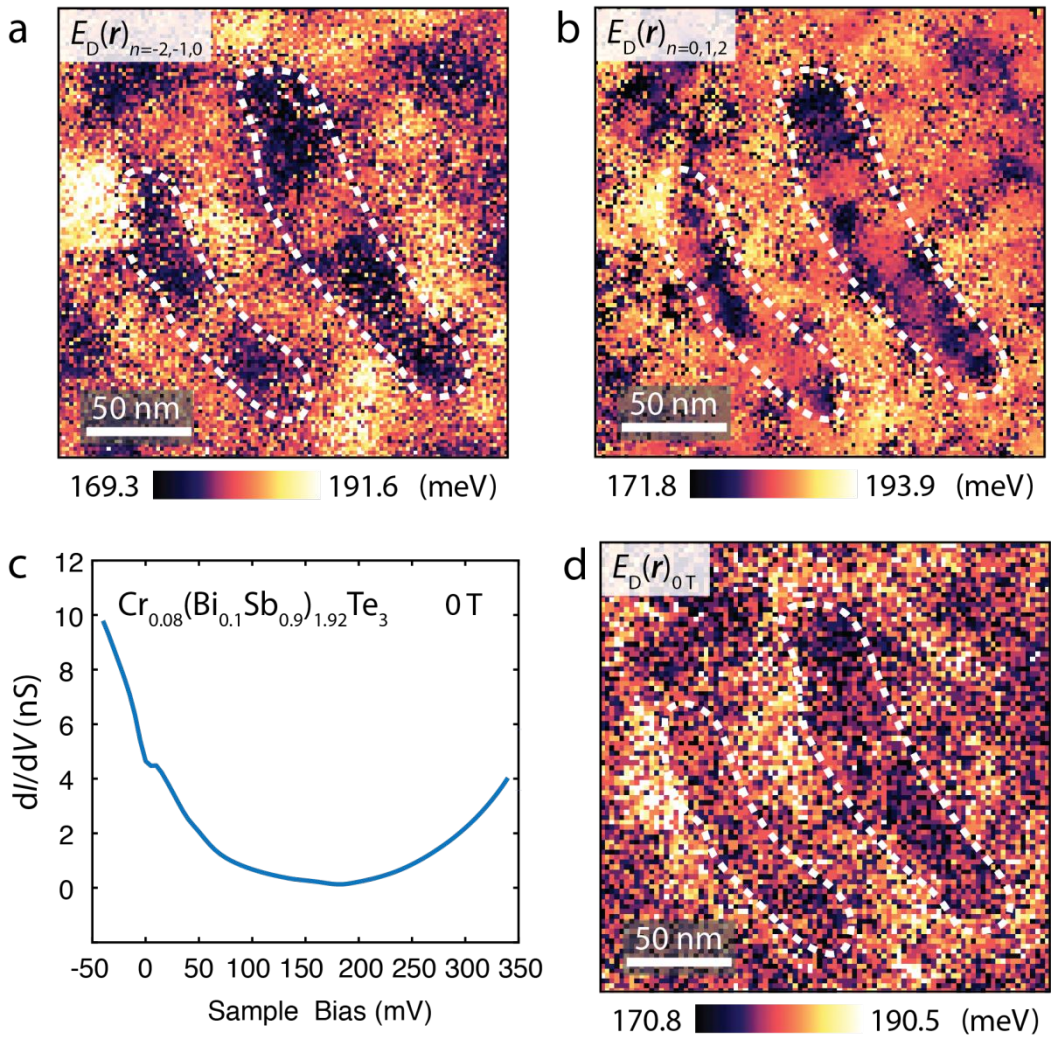


**Figure S7**. Comparison of $E_D(\boldsymbol{r})$ extracted using different LLs and zero magnetic field data. Spatial dependence of the Dirac point $E_D(\boldsymbol{r})$ extracted by using (a) equation (5) with LLs of $n$=-2, -1, 0, (b) equation (9) with LLs of $n$= 0, 1, 2 in an 8.5 T external magnetic field, and (d) the energy of the minimum differential conductance curve (c) in a zero external magnetic field, respectively. Similar features indicated by the dashed curves can be seen in all three images, supporting the validity of using LLs for $E_D(\boldsymbol{r})$ extraction.